Nano-Micro Letters

e-ISSN 2150-5551
CN 31-2103/TB

ARTICLE

https://doi.org/10.1007/s40820-026-02128-5

Cite as
Nano-Micro Lett.
(2026) 18:278

Received: 19 November 2025
Accepted: 4 February 2026

Self-Sensing NiFe@N-doped Carbon Aerogel: Integrating Excellent Radar Stealth, Inherent Structural Health Monitoring, Thermal Management, and Flame Retardancy

Xiaosen Du[1,3], Jianhua Zhou[1,3] ✉, Jiarui Yu[1,3], Xiaoyan Nie[1,3], Mingyu Luo[1,3], Xingyuan He[1,3], Anguo Xiao[2]

HIGHLIGHTS

- The biomimetic honeycomb-like porous magnetic NiFe@N-doped carbon aerogel (NFNCA) was efficiently fabricated through chemical cross-linking, in situ growth, unidirectional freeze-drying, and pyrolysis carbonization.
- The synergistic effect arising from the 3D conductive networking structure, diverse heterogeneous interfaces, magnetic/dielectric multi-component, and multiple loss pathways of NFNCA endowed this carbon aerogel with outstanding impedance matching and electromagnetic wave attenuation performance.
- The NFNCA featured excellent microwave attenuation, real-time monitoring of structural integrity, infrared thermal stealth, thermal management, and flame retardancy capabilities.

ABSTRACT Biomass carbon-based aerogels derived from collagen protofibrils are gaining considerable attention in electromagnetic protection. However, achieving a well-designed microstructure, optimized magnetic and dielectric loss components, and integrated multifunctionality within a single material system remains a significant challenge. Herein, a three-dimensional (3D) hierarchically biomimetic honeycomb-like porous magnetic NiFe@N-doped carbon aerogel (NFNCA) is obtained via a simple strategy involving in situ growth, freeze-drying, and pyrolysis carbonization. Driven by the synergy of a 3D conductive networking structure, magnetic and dielectric multi-components, numerous heterogeneous interfaces, and diverse loss pathways, the optimized NFNCA exhibits exceptional electromagnetic wave attenuation capability, evidenced by a minimum reflection loss (R_L) of −53.49 dB at 1.93 mm and an effective absorption bandwidth of 6.24 GHz (11.76–18.00 GHz). Furthermore, the exceptional radar stealth, infrared thermal stealth, thermal management, and flame retardancy characteristics of NFNCA render it a promising candidate for multiple applications in demanding environments. Interestingly, the 3D cross-linked conductive network of NFNCA can serve as strain sensors to detect changes in the internal structure of carbon aerogels. Hence, this work provides a feasible design strategy for developing lightweight, high-efficiency, and multifunctional biomass-based carbon aerogel electromagnetic wave absorbing materials for various application scenarios.

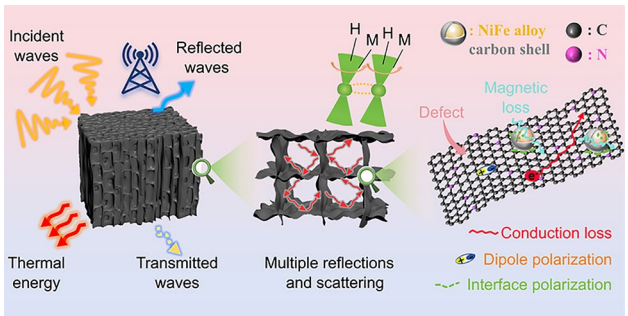

✉ Jianhua Zhou, zhoujianh@21cn.com
[1] College of Bioresources Chemical and Materials Engineering, Shaanxi University of Science and Technology, Xi'an 710021, People's Republic of China
[2] Hunan Provincial Key Laboratory of Water Treatment Functional Materials, Hunan University of Arts and Science, Changde 415000, People's Republic of China
[3] National Demonstration Center for Experimental Light Chemistry Engineering Education (Shaanxi, University of Science and Technology), Xi'an 710021, People's Republic of China

Published online: 10 March 2026

KEYWORDS Biomass-based carbon aerogel; Microwave attenuation; Simulation; Structural integrity monitoring; Multifunction

1 Introduction

The rapid advancement of 5G technology has resulted in unprecedented societal progress and remarkable improvements in human life. Nevertheless, this development has heightened worries about electromagnetic wave (EMW) pollution and posed a potential threat to public health [1–5]. Hence, the design of materials and structures with high-efficiency EMW absorption has garnered considerable attention. To meet the practical demands of advanced electronics (e.g., 5G base stations, smart devices), aerospace, automotive industry, and smart buildings, ideal electromagnetic wave absorbing (EMWA) materials are required to possess not only the "thin, lightweight, broad, and strong" characteristics, but also superior environmental adaptability, such as excellent mechanical properties, thermal insulation, and flame retardancy [6]. Most importantly, real-time structural integrity monitoring has emerged as an indispensable criterion for promptly detecting unforeseen or subtle in-service damage, thereby maintaining the reliability of EMWA materials [7, 8]. Carbon-based materials, including graphene [9], carbon nanofibers [10], carbon nanocages/microspheres [11], and carbon aerogels, are regarded as extremely promising candidates for the development of outstanding EMWA materials. This is attributed to their inherent dielectric characteristics like transported electrons and dipoles, which are predominant in the internal electromagnetic response and energy conversion processes [12]. Moreover, carbon-based materials' unique physical characteristics (e.g., well-developed pore structure, excellent thermal stability, and electrical properties) offer a promising pathway to meet the advanced requirements for environmental adaptability and structural health monitoring. However, synergistically integrating these multiple functionalities into a single, lightweight, and robust structure remains a significant challenge.

Recently, carbon aerogels derived from diverse biomass sources, such as wood [13, 14], cellulose [15–17], chitin [18, 19], and collagen protofibril [20], have attracted significant attention due to their environmental friendliness, widespread availability, abundant functional groups, large specific surface areas, and high porosity. Among these biomass sources, collagen protofibril extracted from leather industry wastes has emerged as an ideal choice, featuring high nitrogen content, numerous polar functional groups, excellent biodegradability and biocompatibility [21–23]. This sustainable strategy reduces reliance on petrochemical materials and mitigates industrial waste disposal pressure. Nitrogen doping can lead to diverse structural defects in the carbon skeleton and alter the distribution of the electron cloud, guiding the generation of electric dipoles under electromagnetic field conditions, which triggers dipole polarization and facilitates the attenuation of EMWs [24]. Although N-doped carbon aerogels derived from collagen protofibrils exhibit great potential for efficient EMW absorption, their fragile mechanical properties remain a primary challenge, limiting the application in complex practical environments. Cross-linking the collagen protofibril with various agents, such as glutaraldehyde [25], tannic acid [26], and metal ion [27], prior to heat treatment is a key strategy to fortify the network and thus enhance the mechanical properties of the final carbon aerogel. However, the EMW attenuation capability of modified collagen protofibril-based carbon aerogels still remains unsatisfactory due to the single dielectric loss mechanism. The synergistic electromagnetic loss effect of dielectric/magnetic hybrid materials can diversify loss mechanisms and optimize impedance matching, thereby enhancing the EMW attenuation capability [28, 29]. Magnetic components can be generated through carbonization of metal–organic frameworks (MOFs) [29, 30], which offer notable advantages including adjustable porosity, high dispersibility, easy component adjustability, and strong magnetization. In comparison with other MOFs, magnetic particles derived from Prussian blue analogues (PBAs) leverage extra advantages, such as higher metal content, readily tunable metal species, and smaller particle size, making them more conducive to enhancing magnetization and electromagnetic compatibility [31–33]. However, the conventional ex situ compositing method (mechanical blending) often results in poor interfacial compatibility between MOFs (including PBAs) and carbon matrix. This leads to a non-uniform distribution of the MOF-derived phases, generating agglomerated and isolated conductive islands that impair the EMW attenuation capability [34]. A more effective "bottom-up" approach, anchoring MOFs onto polymer backbones such as cellulose [35] and chitosan [36] prior to gelation, has been proven highly effective. However, to the best of our knowledge, no study has yet reported a strategy that utilizes in situ growth of MOFs within collagen

 https://doi.org/10.1007/s40820-026-02128-5

protofibrils to fabricate high-performance, multifunctional magnetic carbon aerogels with desirable interfacial connectivity and uniform particle dispersion.

Herein, we reported an extensible strategy utilizing dialdehyde cellulose nanofibril (DCNF) as a cross-linking agent to fabricate biomimetic honeycomb-like porous magnetic NiFe@N-doped carbon aerogel (NFNCA) through simple in situ growth, unidirectional freeze-drying, and pyrolysis carbonization. Through a facile chemical cross-linking approach, the formation of Schiff base covalent bonds between DCNF and collagen protofibrils could promote the construction of a three-dimensional (3D) network structure, providing favorable conditions for establishing a robust carbon aerogel skeleton. The abundant functional groups (e.g., carboxyl, amino, hydroxyl, amide, and imine groups) within the DCNF-crosslinked collagen protofibril network endowed it with a unique capacity for interfacial interactions, enabling it to coordinate with metal ions to form robust interfacial bonds. The in situ growth of NiFe-PBA particles within the DCNF-crosslinked collagen protofibril network resulted in a magnetic carbon aerogel featuring low density, high magnetic nanoparticle dispersion, strong interfacial connectivity, and superior mechanical properties. Significantly, the electrical conductivity, magnetism, and EMW attenuation capability of the NFNCAs could be readily obtained by adjusting the loading content of NiFe-PBA particles. The optimized sample exhibited excellent EMW attenuation capability, with a minimum reflection loss (R_L) of −53.49 dB achieved at 1.93 mm and a wide broad effective absorption bandwidth (EAB) of 6.24 GHz obtained at 1.60 mm. In addition, NFNCAs exhibited real-time structural integrity monitoring, exceptional infrared thermal stealth, thermal management, and flame retardancy capabilities. This work opens new avenues for future exploration of high-performance multifunctional biomass-based carbon aerogels and the NFNCA demonstrates significant prospects for application in diverse fields, such as next-generation electronics, specialized equipment protection, aerospace, and defense applications.

2 Experimental Section

2.1 Fabrication of DCNF

DCNFs rich in aldehyde functional groups were prepared by the selective oxidation of cellulose nanofibrils (CNFs) with $NaIO_4$. The aldehyde content of DCNF was 3.48 ± 0.15 mmol g^{-1} as determined by the hydroxylamine hydrochloride/sodium hydroxide method. Detailed experimental processes are available in Sects. 1.2 and 1.3 of the Supporting Information.

2.2 Fabrication of NiFe@N-doped Carbon Aerogel

The preparation process of NiFe@N-doped carbon aerogel (NFNCA) is displayed in Fig. 1a. The DCNF content could affect the mechanical properties, density, and porosity of NFNCA. According to Fig. S1, when the DCNF content was 45 wt% of collagen protofibril, the comprehensive performance of NFNCA was optimal. Specifically, 0.2343 g of collagen protofibril and 0.1054 g of DCNF were dispersed in 25 mL of deionized water and stirred for 2 h to form mixture A. Then, 0.0776 g of $Ni(NO_3)_2{\cdot}6H_2O$ and 0.1177 g of $Na_3C_6H_5O_7{\cdot}2H_2O$ were dissolved in 5 mL of deionized water. The resulting solution was mixed with half of mixture A and subsequently magnetically stirred at 500 rpm for 15 min to yield suspension B. Similarly, 5 mL of deionized water was used to dissolve 0.0585 g of $K_3Fe(CN)_6$. The resultant solution was then mixed with the remaining mixture A under magnetic stirring at 500 rpm for 15 min to yield suspension C. Subsequently, suspension B was quickly poured into suspension C and magnetically stirred at 500 rpm for 15 min. Then, the resultant mixture was transferred into a specially designed Teflon mold with a copper base, followed by standing at room temperature for 24 h to enable the in situ growth of NiFe-PBA particles. To create a directional temperature differential, the mold was placed on the surface of a copper column immersed in liquid nitrogen for unidirectional freezing until the suspension was completely frozen. Subsequently, the NiFe-PBA/collagen protofibril composite aerogels (NFPAs) were produced via freeze-drying at −55 °C for 72 h. By adjusting the content of metal salts (27.2, 42.8, or 59.9 wt%), NFPAs with different NiFe-PBA contents were synthesized and designated as NFPA-1, NFPA-2, and NFPA-3, respectively. Finally, the NFPAs were put in a quartz boat and heated to 650 °C under an Ar atmosphere for 2 h with a heating rate of 5 °C min^{-1} to obtain NFNCAs, which were denoted as NFNCA-1, NFNCA-2, and NFNCA-3, respectively. For comparison, NFPA-0 without metal salts and its pyrolyzed product

NFNCA-0 were prepared following the same procedure as described above.

3 Results and Discussion

3.1 Morphology and Structure

The fabrication process of NiFe@N-doped carbon aerogel involved the in situ synthesis of NiFe-PBA particles within a DCNF-crosslinked collagen protofibril network, following unidirectional freeze-drying and pyrolysis carbonization processes (Fig. 1a). Initially, the Schiff base reaction occurred between the amino groups of collagen protofibrils and the aldehyde groups of DCNF (Fig. S2), thereby generating a cross-linked network structure. The DCNF-crosslinked collagen protofibril network had a large number of carboxyl, amino, hydroxyl, amide, and imine groups, which made it possible for Ni^{2+} ions to interact with the network directly. Meanwhile, Ni^{2+} ions within the DCNF-crosslinked collagen protofibril network formed complexes with ferrocyanide ions, through which the NiFe-PBA nuclei were anchored onto the DCNF-crosslinked collagen protofibril network and continuously grew into NiFe-PBA particles. The formation of a coordination complex between the DCNF-crosslinked collagen protofibril network and NiFe-PBA particles could be confirmed by the blue shift of the characteristic peak corresponding to the associated hydroxyl groups (-OH) in the Fourier transform infrared (FTIR) spectra (Fig. S3). Finally, the rigid NiFe-PBA particles were firmly anchored within the DCNF-crosslinked collagen protofibril network via strong interfacial coordination bonds, forming a stable 3D cross-linked system. In addition, the zeta potential of composite dispersion increased progressively with the NiFe-PBA loading content (Fig. S4), indicating that in situ growth of NiFe-PBA particles enhanced colloidal stability. This drove the formation of the jelly-like gel (Fig. S5).

During the freezing phase, the unidirectional ice crystals acted as templates, and the NiFe-PBA/DCNF-crosslinked collagen protofibril hybrids was excluded by the growing ice crystals, allowing them to aggregate between ice crystals and form directional pore walls [37, 38]. Therefore, the NFPAs achieved an anisotropic pore structure after freeze-drying. The SEM image (Fig. 1b) revealed that NFPA possessed aligned cell walls, along with interconnected "bridges" between the parallel lamellae. NiFe-PBA particles existed in NFPA and were uniformly distributed (Fig. 1c). The surrounding matrix partially covered the NiFe-PBA particles, indicating that the nanocrystals were effectively embedded in the NFPA walls with good interfacial connectivity. Especially, NFPA presented a typical honeycomb-like biomimetic structure in transverse section (Fig. 1d). The X-ray diffraction (XRD) patterns of NiFe-PBA particles and NFPAs were consistent with those of standard pattern of $K_2FeNi(CN)_6$ (PDF#20–0915), which confirmed the successful synthesis of NiFe-PBA particles within NFPAs (Fig. 1e). In terms of morphology, after carbonization, the cell walls of the absorber became more curved and wrinkled, and the average pore gap decreased while the directional pore structure was reserved (Fig. 1f). Moreover, the energy-dispersive spectroscopy (EDS) element mapping indicated that N, O, Ni, and Fe elements in NFNCA-2 were well distributed (Fig. 1g-j), which implied that the in situ growth of NiFe-PBA on the carbon matrix was uniform. NiFe alloy nanoparticles with approximately sphere-like morphology and about 57 nm in diameter were observed to be embedded in the amorphous carbon matrix, as visualized by low-resolution transmission electron microscope (TEM) (Fig. 1k). Moreover, the high-resolution TEM image clearly revealed that the lattice spacing of the crystalline metal particles was 0.205 nm (Fig. 1l). Furthermore, the selected area electron diffraction (SAED) pattern (Fig. 1l inset) revealed the crystal planes (111), (200), and (220) of the NiFe alloy, which was also confirmed in XRD pattern (Fig. 2a) [39]. Overall, the embedding of these crystalline NiFe alloy nanoparticles within the carbon matrix generated abundant heterogeneous interfaces. These interfaces acted as polarization centers, facilitating charge accumulation and thereby significantly enhancing the EMW attenuation capability.

The crystalline structure of the NFNCAs was investigated by XRD, revealing three distinct diffraction peaks at $2\theta = 44.14°$, 51.28°, and 75.37° (Fig. 2a). These diffraction peaks, respectively, corresponded to the (111), (200), and (220) planes of the NiFe alloy (PDF#03–1109). Additionally, a broad diffraction peak was detected between 20° and 25°, indicating the existence of graphite carbon. The absence of impurity peaks indicated that NiFe@C nanoparticles possessed good crystallinity and stability, which stemmed from the protection provided by the

 https://doi.org/10.1007/s40820-026-02128-5

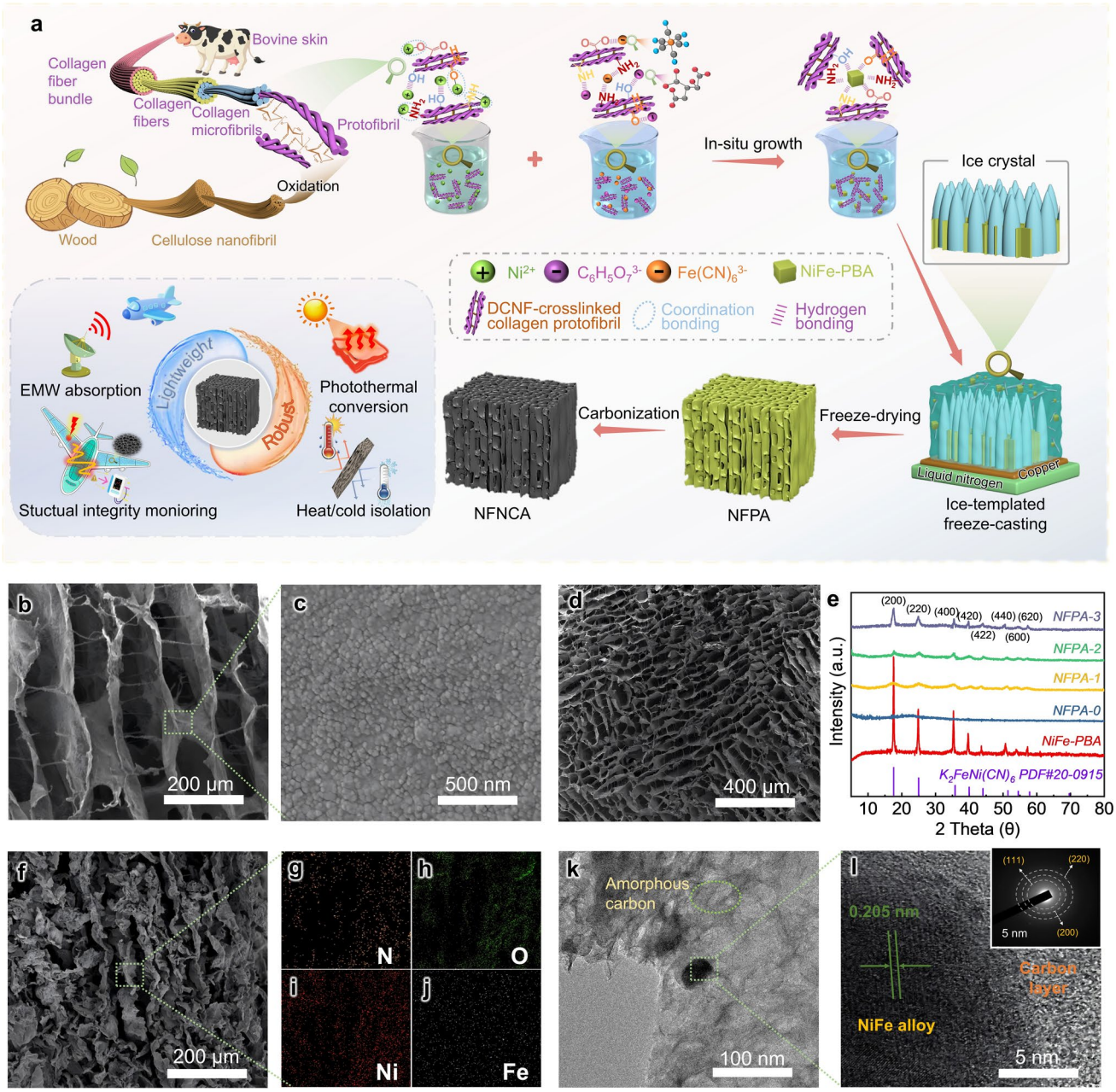

Fig. 1 **a** Schematic diagram of fabricating NFNCA for multifunctional applications. **b** SEM image of NFPA-2 in the longitudinal section. **c** SEM image of in situ grown NiFe-PBA particles in NFPA-2. **d** SEM image of NFPA-2 in the transverse section. **e** XRD spectra of NiFe-PBA particles and NFPAs with different metal salt contents. **f** SEM image of NFNCA-2 in the longitudinal section. **g-j** EDS mapping images of N, O, Ni, and Fe elements. **k** TEM, **l** HR-TEM and selected area electron diffraction (SAED) of NFNCA-2

graphite carbon shell. To analyze the lattice defects in the NFNCAs, Raman spectroscopy was utilized. The spectra of all samples obviously presented two distinct peaks: the D band (1350 cm^{-1}) and the G band (1590 cm^{-1}). The D band is caused by the disordered arrangement of carbon atoms in the carbon framework, while the G band originates from all carbon sites with sp^2 hybridization, including graphitic and non-graphitic sites. The intensity ratio of D band to G band (I_D/I_G) is typically employed as a metric for evaluating the relative graphitization degree of carbon

materials [40, 41]. As the NiFe-PBA loading increased, the I_D/I_G value rose (Fig. 2b), implying the presence of smaller sp^2 carbon nanocrystallites and more lattice defects, which was beneficial for dipole polarization. In this case, the fragmented graphite crystals led to a partial shift in electron migration's conduction mode to electron hopping, which consequently reduced the electrical conductivity (Fig. S6). This was because NiFe-PBA was abundant in N atoms. N atoms had a similar atomic structure to that of C atoms, which promoted the doping of N atoms into the carbon matrix. As a result, the doped N atoms impaired the ordered structure of the graphitic carbon, forming defective structures and disordered carbon [42]. Functioning as potent polarization centers, these induced defects significantly intensified dipole polarization, hence elevating the overall EMW attenuation capability [43].

The elemental composition, chemical bonds, and oxidation states of NFNCA-0 and NFNCA-2 were analyzed by X-ray photoelectron spectroscope (XPS) (Figs. 2c-f, S7, and S8). In the analysis of full-spectra, NFNCA-0 appeared characteristic peaks of C, O, and N elements, and NFNCA-2 showed typical peaks of C, O, N, Ni, and Fe elements (Figs. S7a and S8a). The N 1*s* spectrum of NFNCA-2 revealed three deconvoluted peaks, which were attributed to graphitic N, pyrrolic N, and pyridinic N at binding energies of 401.51, 400.06, and 398.40 eV, respectively. However, for NFNCA-0 without NiFe-PBA, only pyrrolic N (400.89 eV) and pyridinic N (398.40 eV) peaks could be observed (Fig. 2c). This difference was because NiFe-PBA contained numerous cyano (-CN) groups, and the NiFe alloys acted as catalysts to promote the graphitization recombination of -CN groups during high-temperature carbonization, forming sp^2 hybridized graphitic N [44]. Furthermore, the relative peak areas were used to calculate the relative amounts of each nitrogen species in both samples (Table S1). In NFNCA-0, the proportions of pyridinic N and pyrrolic N were 46.51 and 53.49 wt%, respectively, while in NFNCA-2, those of pyridinic N, pyrrolic N, and graphitic N were 51.56, 33.57, and 14.87 wt%, respectively. Pyridinic N favors the generation of lattice defects, pyrrolic N facilitates dipole polarization, and graphitic N can reduce the electrical conductivity of the carbon matrix [45–47]. Therefore, the synergistic effect of these three nitrogen species doped in carbon matrix contributed to the EMW absorption properties of NFNCA-2. The high-resolution Ni 2*p* and Fe 2*p* spectra of NFNCAs were analyzed to determine the elemental valence states. In the Ni 2*p* spectrum (Fig. 2d), the peaks positioned at 853.46 and 870.76 eV were assigned to metallic Ni (Ni^0), while those located at 856.25 and 873.55 eV were associated with oxidized Ni species (e.g., Ni^{2+}). Similarly, the Fe 2*p* spectrum revealed the coexistence of metallic Fe (Fe^0) at 705.36 and 718.46 eV, and oxidized Fe species at 709.92 and 723.52 eV (Fig. 2e). These results confirmed that Ni and Fe in NiFe-PBA were reduced to form alloy particles, which was consistent with the previously presented TEM and XRD results (Figs. 1k, l and 2a). Simultaneously, the oxidation states of the metal elements revealed that alloy particles experienced slight oxidation on their surfaces upon air exposure, a phenomenon that was very common in MOF-derived materials [31]. The C 1*s* spectra of NFNCA-0 and NFNCA-2 could be deconvoluted into four peaks located at 284.80, 285.52, 286.60, and 288.83 eV. These peaks corresponded to C–C/C = C, C–N, C–O, and O–C = O, indicating the existence of various carbon-containing functional groups in the carbon matrix (Figs. S7b and 2f). The O 1*s* XPS spectra of NFNCA-0 and NFNCA-2 were congruous (Figs. S7c and S8b), both revealing three oxygen species attributed to O–C (531.81 eV), C–O–C (533.34 eV), and adsorbed water molecules (536.33 eV).

Based on the IV-type N_2 adsorption–desorption isotherm, some pores were found in NFNCA-2 (Fig. 2g). This pore structure was mainly attributed to the imperfection of the carbon lattice, which was quite common in biomass-derived amorphous carbon. Moreover, the unidirectional structure of the carbon aerogel also influenced the formation of pores. According to the Maxwell–Garnett theory (Eqs. S3 and S4) [35], the air introduced into the pores could reduce the effective dielectric constant, which improved the absorber's impedance matching, thereby enhancing the EMW attenuation capability.

The magnetic properties of NFNCA-0 and NFNCA-2 were characterized by VSM, and the hysteresis lines are shown in Fig. 2h, i. Compared with NFNCA-0, NFNCA-2 exhibited an obvious symmetrical hysteresis loop, indicating that the introduction of NiFe-PBA particles endowed the absorber with good ferromagnetic behavior. The saturation magnetization strength (M_S) and coercivity (H_c) of NFNCA-2 were 13.04 emu g^{-1} and 41.11 Oe, respectively. Due to the presence of the non-magnetic carbon matrix, these values were lower than those of bulk NiFe alloys (about 87.3 emu g^{-1} and 353 Oe) [39]. The lower coercive force weakened the magnetic anisotropy and thereby caused the natural resonant frequency to shift toward lower frequencies, which was beneficial for the

https://doi.org/10.1007/s40820-026-02128-5

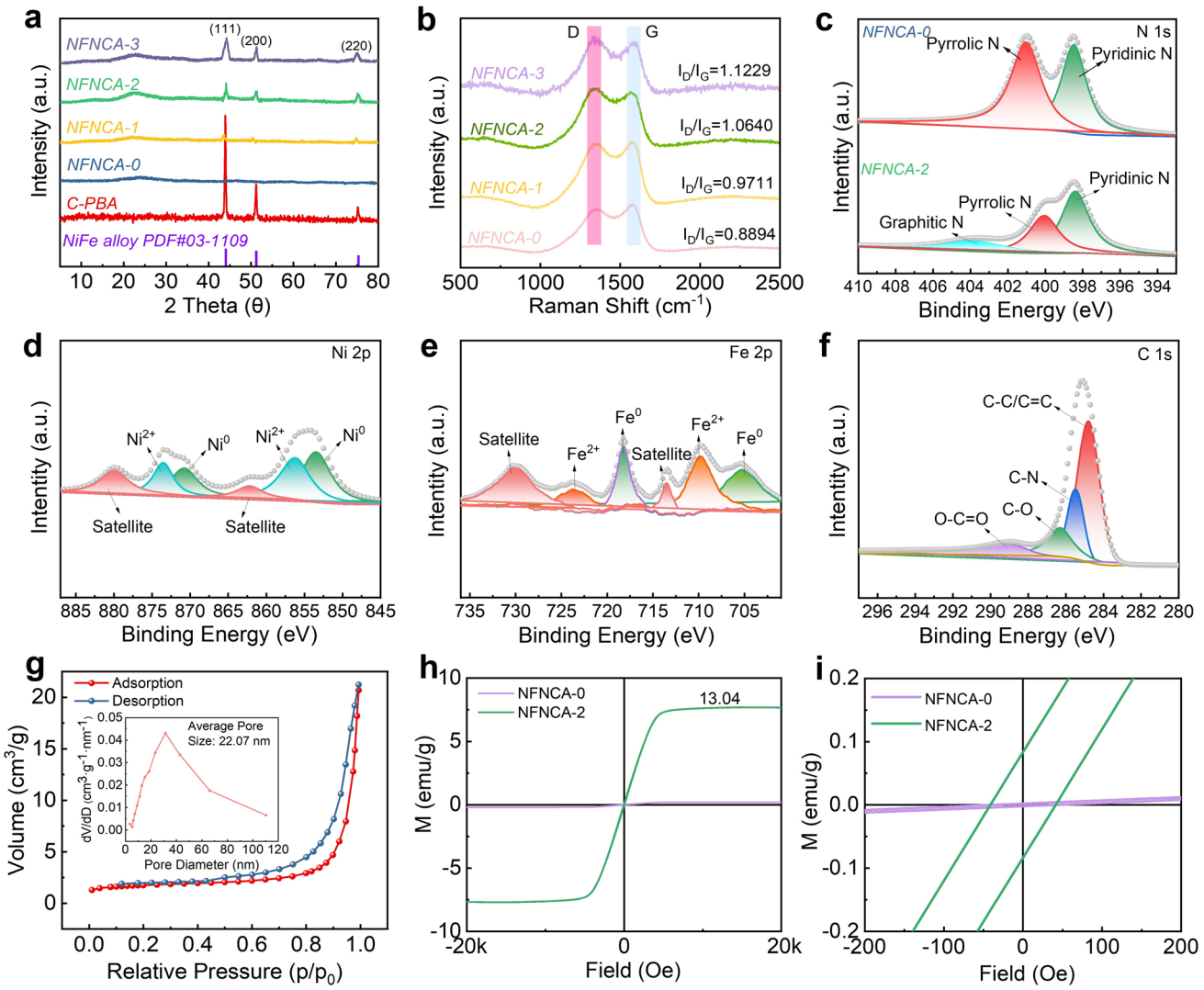

Fig. 2 **a** XRD patterns of the NFNCAs and carbonized NiFe-PBA (C-PBA). **b** Raman spectra of the NFNCAs with different NiFe-PBA contents. **c** N 1*s* XPS spectra of NFNCA-0 and NFNCA-2. **d-f** Ni 2*p*, Fe 2*p*, and C 1*s* XPS spectra of NFNCA-2. **g** N_2 adsorption–desorption isotherms of NFNCA-2. **h-i** Hysteresis lines and their local magnification diagram of NFNCA-0 and NFNCA-2

attenuation of EMWs in the low-to-medium frequency range (Eqs. S5-S7).

3.2 EMW Absorption Performance of NFNCAs

According to the transmission line theory (Eqs. S8 and S9), the widely used evaluation indicators for the EMW attenuation capability of absorbers include the R_L value and the EAB value. In general, an R_L value less than −10 dB indicates that more than 90% of the incident EMW energy is absorbed, and the corresponding frequency band with $R_L < -10$ dB is considered as the EAB. NFNCA-0 exhibited relatively weak EMW absorption capability, with a minimum R_L value of −14.61 dB (t = 0.88 mm, f = 15.55 GHz) and an EAB of 1.43 GHz (t = 0.88 mm, 14.81–16.24 GHz) (Fig. S9), which might be caused by its poor impedance matching characteristics (Fig. S16a, impedance matching diagram). In contrast, after introducing NiFe-PBA, the EMW attenuation capability of NFNCAs was significantly improved (Figs. 3a-c and S10-S12), indicating that the in situ grown NiFe-PBA had a positive effect on enhancing EMW absorption. Among them, NFNCA-1 achieved a minimum R_L value of −31.74 dB (t = 1.30 mm, f = 17.92 GH) and an

EAB of 3.99 GHz (t = 1.49 mm, 14.00–17.99 GHz) (Figs. 3a and S10). Notably, the minimum R_L value of NFNCA-2 reached −53.49 dB (t = 1.93 mm, f = 11.44 GHz) (Figs. 3b and S11a). According to Eq. S10, NFNCA-2 could attenuate more than 99.99955% of EMW energy. Meanwhile, the EAB of NFNCA-2 reached 6.24 GHz (t = 1.60 mm, 11.76–18.00 GHz), covering the entire X-band (Fig. S11b). However, further increasing the NiFe-PBA loading content resulted in a decrease in EMW absorption performance. For instance, NFNCA-3 exhibited a minimum R_L value of −15.04 dB (t = 3.92 mm, f = 12.96 GHz) and an EAB of 2.82 GHz (t = 4.33 mm, 11.09–13.91 GHz) (Figs. 3c and S12), indicating that excessive NiFe alloy nanoparticles may hinder the construction of the 3D conductive network structure. NFNCA-2 demonstrated advantages in both absorption intensity and bandwidth (Fig. 3d), suggesting that a reasonable loading content of NiFe-PBA was crucial for achieving optimal EMW absorption capacity. Therefore, the EMW attenuation ability of NFNCAs could be regulated by tuning the loading content of NiFe-PBA. Furthermore, as thickness increased, the NFNCA-2 absorption frequency shifted toward lower frequencies, which could be described by the quarter-wavelength (1/4λ) cancellation theory (Eq. S11). The experimental t_m perfectly matched the theoretically estimated values, indicating the presence of interference-type loss in NFNCA-2 (Fig. S13) [64]. In summary, NFNCA-2 exhibited EMW absorption with selectivity of frequency. When the incident EMW frequency matched resonance frequency of the material, it would present maximum interference loss and optimal EMW attenuation capability.

To better explore the electromagnetic characteristics of NFNCAs, the dielectric constant ($\varepsilon_r = \varepsilon' - j\varepsilon''$) and permeability ($\mu_r = \mu' - j\mu''$) were also studied. The real parts (ε', μ') denote the ability to storage electromagnetic energy, while the imaginary parts (ε'', μ'') represent the ability to dissipate electromagnetic energy [65]. The decrease in permittivity with increasing frequency (Fig. 3e), which indicates that the EMW attenuation process was mostly influenced by conductive losses [10]. Electromagnetic parameters (ε', ε'', μ', and μ'') of NFNCAs could be regulated by NiFe-PBA content. As compared with NFNCA-0, the introduction of NiFe-PBA particles reduced the complex permittivity. In contrast, the complex permeability increased as the NiFe-PBA content enhanced (Fig. 3f). However, the magnetic loss tangent ($\tan\delta_\mu$) remained significantly lower than the dielectric loss tangent ($\tan\delta_\varepsilon$) across all loading levels (Fig. S14a, b), demonstrating that dielectric properties dominated EMW absorption.

To elucidate the underlying dielectric loss mechanisms, Cole–Cole analysis was performed. It could be clearly separated between contributions from conduction loss and polarization loss processes (Eq. S12). The presence of semicircles shows the polarization loss process, and the slope of the curve's tail represents the conduction loss of samples. In the Cole–Cole plot (Fig. 3g), the upward tendency was not observed for NFNCAs with high NiFe-PBA loading content (NFNCA-2 and NFNCA-3), which indicated that NiFe alloy nanoparticles could inhibit the electrical conductivity (Fig. S6) [66]. A linear relationship between ε' and ε''/f indicated that dipole polarization was the only dielectric loss process (Eq. S13). The relationship was nonlinear (Fig. 3h), which confirmed that both dipole and interfacial polarization processes existed in NFNCAs [67].

Furthermore, based on Debye theory, the imaginary part of permittivity is separated into two parts ($\varepsilon'' = \varepsilon_c'' + \varepsilon_p''$), with ε_c'' representing the conduction loss and ε_p'' representing the polarization loss (Eq. S14) [68]. The nonlinear least squares method was used to fit the conduction loss and polarization loss. Regardless of varying NiFe-PBA loading contents, the ε_c'' remained significantly larger than the ε_p'', demonstrating that conduction loss played a dominant role in the overall dielectric loss (Fig. S15). This was because the NFNCAs formed a conductive network within the paraffin matrix, resulting in increased conductive loss, which facilitated the conversion of EMW energy into thermal energy [69]. Regarding ε_p'', there existed multiple relaxations for NFNCAs. Specifically, ε_p'' mainly originated from polarization relaxation of functional groups and defect dipoles in NFNCAs. The enhancement of interfacial polarization resulted from the existence of unbalanced charge accumulation at the interface between the surface of NFNCA and NiFe-PBA, forming a capacitor-like structure, which was conducive to the dielectric polarization response [70]. Thus, the aforementioned-findings further confirmed the influence of three primary factors of interfacial polarization relaxation, defect dipole polarization relaxation, and conductive loss on the dielectric loss of the NFNCAs.

To elucidate the contribution of eddy current loss in the magnetic loss mechanism of NFNCAs, the C_0 criterion (Eq. S15) was evaluated on the basis of the skin effect theory [71]. Theoretically, if magnetic loss is only caused by eddy

https://doi.org/10.1007/s40820-026-02128-5

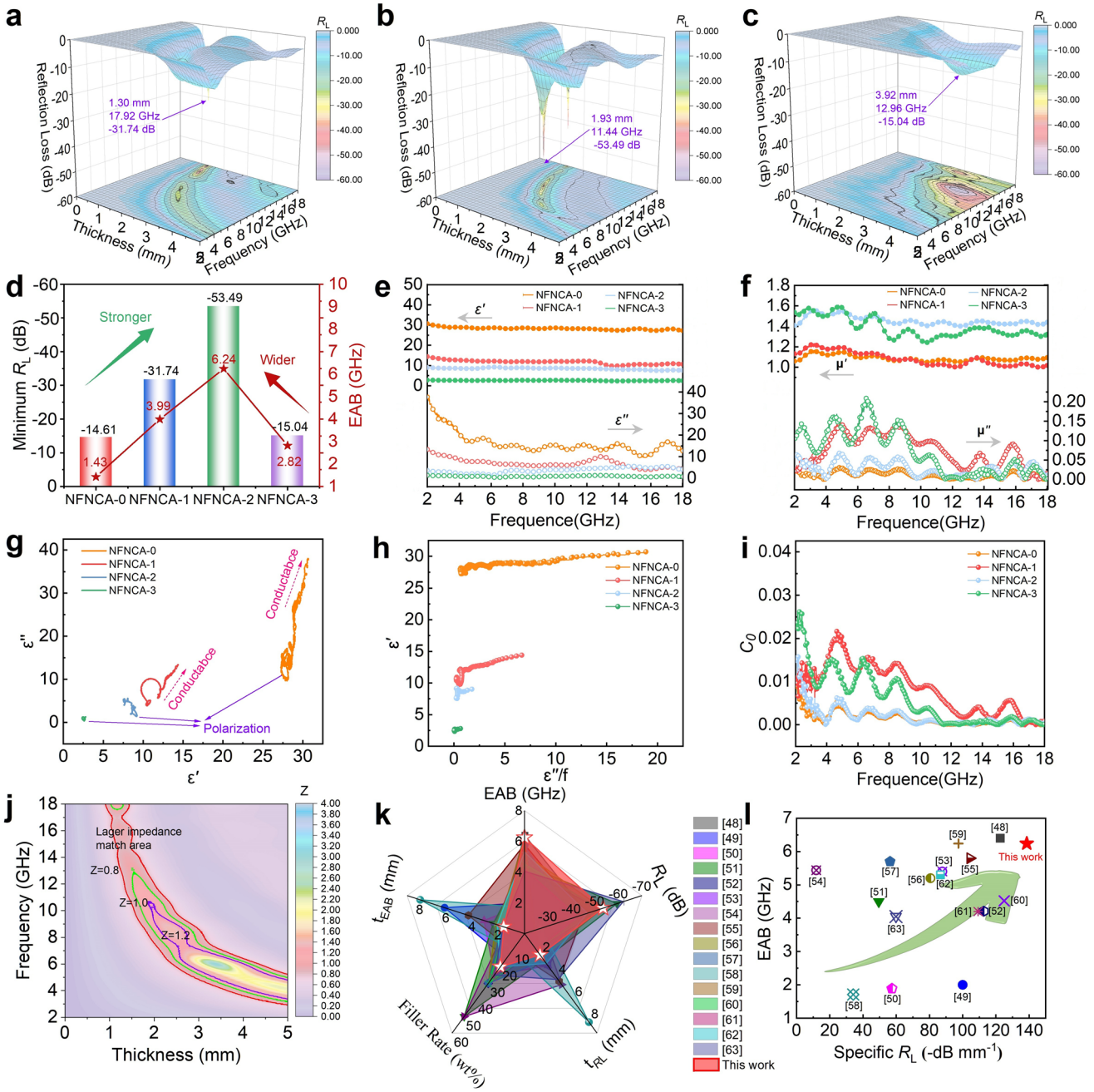

Fig. 3 EMWA performance of **a** NFNCA-1, **b** NFNCA-2, and **c** NFNCA-3. **d** Comparison of the minimum R_L and EAB between samples. **e** ε' and ε'' values for NFNCAs. **f** μ' and μ'' values for NFNCAs. **g, h** Cole–Cole picture and the relationship between ε' versus ε''/f of NFNCAs. **i** Eddy current loss of NFNCAs. **j** Two-dimensional pattern of impedance values of NFNCA-2. **k** EMWA characteristics of NFNCA-2 compared with the reported carbon-based composites [48–63]. **l** Specific R_L value of NFNCA-2 compared with previously reported works

current loss, the C_0 values should remain constant across the measured frequency range. In contrast, the C_0 values show notable fluctuations if magnetic loss is mostly driven by ferromagnetic resonance. The magnetic loss of NFNCAs consisted of natural resonance (2–10 GHz) and exchange resonance (10–18 GHz) (Fig. 3i). Meanwhile, the absence of flat regions in the C_0 curves confirmed the absence of eddy current loss, which was mainly attributed to the tiny particle size of NiFe alloys [66].

Impedance matching (Z, Eq. S16) and attenuation constant (α, Eq. S17) are key factors for assessing EMW absorption capabilities. In general, impedance matching can be assessed using $Z=|Z_{in}/Z_0|$, and a Z-value within the range of 0.8–1.2 is regarded as exhibiting ideal impedance matching performance [72]. The Z-value graph of NFNCA-0 (Fig. S16a) showed that the impedance matching was poor, which was due to high electrical conductivity causing EMW reflection. In contrast, the introduction of NiFe-PBA and the formation of numerous heterogeneous interfaces in the carbon matrix led to the reduction of NFNCA electrical conductivity. Therefore, NFNCAs demonstrated enhanced impedance matching capabilities (Figs. 3j and S16b, c). Notably, NFNCA-2 exhibited the biggest ideal impedance matching region (Fig. 3j), suggesting that the employed strategy efficiently optimized impedance matching. Furthermore, the EMW attenuation capacity of EMWA materials is demonstrated by the α (Eq. S17) [73]. The value of α followed the order of NFNCA-0 > NFNCA-1 > NFNCA-2 > NFNCA -3 across the entire test frequency range (Fig. S17), which indicated that NFNCA-0 possessed the most effective EMW attenuation capability. Nevertheless, the excessive dielectric loss in NFNCA-0 induced the significant impedance mismatch, resulting in unsatisfactory EMW attenuation capability. In comparison with the EMWA materials in the previous literature (Table S2), NFNCA-2 demonstrated the wide EAB of 6.24 GHz, strong absorption of −53.49 dB and low filler rate (20 wt%), as shown in radar chart (Fig. 3k). Moreover, specific reflection loss (specific R_L, calculated via Eq. S18) is usually used to explain the minimum R_L value *vs* thickness and filler rate, and can evaluate the material's comprehensive advantages in terms of light weight, thin thickness, and efficient absorption properties [18]. While maintaining a wide EAB, the specific R_L value in this work reached −138.58 dB mm^{-1}, which indicated that the EMW attenuation capability of the biomimetic honeycomb-like porous magnetic NFNCA was superior to that of most EMWA materials reported previously (Fig. 3l and Table S2).

3.3 Electromagnetic Simulation Results and EMW Attenuation Mechanism of NFNCAs

To assess the EMW absorption capacity of NFNCAs minimum R_L actual far-field conditions, RCS simulations of perfect electric conductor (PEC) plates coated with NFNCA-0, NFNCA-1, NFNCA-2, and NFNCA-3 were performed using CST software (Fig. 4a-h). In this simulation model, the positive Z axis was defined as the direction of incidence, while theta represented the detection angle (Fig. 4a). Other simulation parameters were provided in Sect. 1.5 of the Supporting Information. The 3D simulated color maps and 2D RCS values of a PEC plate and PEC plates coated with NFNCAs between -90° to 90° are exhibited in Fig. 4b-f. The PEC plate exhibited the maximum radar scattering intensity, whereas PEC plates coated with NFNCAs showed significant reductions in radar scattering intensity, confirming the NFNCAs' exceptional omnidirectional EMW absorption capability. The RCS values steadily dropped from 0° to ± 90° with several oscillations as the detection angle deviated (Fig. 4g). Compared to the PEC plate and other NFNCAs/PEC samples, NFNCA-2/PEC consistently exhibited the lowest RCS values (< −10 dB m^2) throughout the −90° to 90° angular range, which corresponded well with its prominent EMW absorption performance (Fig. 3d). To corroborate the preceding statement, Fig. 4h shows a bar chart comparison of the RCS reduction values (the RCS values of PEC plate minus those of the samples). The NFNCA-2/PEC model exhibited the highest RCS reduction value of 29.82 dB m^2 at 30°. The above results demonstrated that NFNCA-2 was effective in absorbing radar waves, resulting in excellent radar stealth capabilities.

The COMSOL finite-element method was employed to simulate the distribution of electric field intensity, magnetic field intensity, surface current density, and power loss density of NFNCA-2 (Fig. 4i). The distributions of the electric and magnetic fields at 11.44 GHz were illustrated in Fig. 4j, revealing that the electric field was primarily focused on the top, whereas the magnetic field was primarily distributed at the bottom region. Particularly, the power loss density distribution was consistent with the electric field distribution, which demonstrated that the attenuation effect of dielectric loss on EMWs was significant. The frequency at the minimum R_L point corresponded to the frequency at a high attenuation constant and Z = 1 (Fig. 4k). NFNCA-2 exhibited an outstanding EMW absorption capacity, confirming that simultaneous achievement of favorable impedance matching and strong attenuation was essential for superior EMW absorption performance. Surface current density and power loss density simulations of NFNCA-2 were conducted at frequencies of 3, 6, 11.44, and 17 GHz, respectively (Fig. 4k inset). Surface current density directly

 https://doi.org/10.1007/s40820-026-02128-5

correlated with impedance matching characteristics, while power loss density reflected the attenuation capacity of the absorber (corresponding to α). Higher power loss density indicated enhanced EMWs energy dissipation. Evidently, the power loss density at 11.44 GHz exceeded those at 3, 6, and 17 GHz, which was in line with the evolving trend of EMW absorption performance (Figs. 3b and S11a). However, excessive surface current density at 17 GHz caused reflection, hindering the entry of EMWs and consequently reducing power loss density. This observation further substantiated that optimal impedance matching served as a critical prerequisite for achieving outstanding EMW attenuation capability.

Based on the above analysis, the schematic illustration of the proposed EMW attenuation mechanism of NFNCAs is presented in Fig. 4l. Firstly, the hierarchical porous structure of NFNCAs, combined with the uniform dispersion of NiFe alloy within the carbon matrix, synergistically optimized impedance matching conditions. This facilitated the penetration of incident EMWs into the material and enabled multiple reflections and scatterings of EMWs within the internal spatial framework of NFNCAs, thereby enhancing EMW attenuation. Secondly, the conduction loss resulted from the activation of conductive carriers that migrated along the conductive network of NFNCAs under alternating electromagnetic field excitation. This process finally transformed EMW energy into thermal energy [74]. Thirdly, the structural defects originating from residual functional groups and nitrogen doping within the carbon matrix served as dipole centers under the influence of an electromagnetic field, thus inducing dipole polarization [75–77]. The numerous heterogeneous interfaces formed between NiFe alloy nanoparticle cores and carbon shells facilitated charge accumulation, leading to interfacial polarization [78–80]. Finally, magnetic loss contributions from NiFe alloy nanoparticles enhanced the overall attenuation performance. Thus, the synergistic integration of these multiple attenuation mechanisms enabled NFNCAs to exhibit exceptional EMW absorption performance.

3.4 Real-Time Monitoring of Structural Integrity

Interestingly, the 3D cross-linked conductive network of NFNCA could serve as strain sensors to detect changes in the internal structure of NFNCA. As demonstrated in Fig. 5a, the longitudinal resistance of NFNCA-2 remained constant without external force applied. When pressure was slowly applied and released with fingers, the electrical signal decreased or increased accordingly (Fig. 5b). Real-time electrical signal measurement enabled the detection of NFNCA plastic deformation and structural damage. As the compressive strength of NFNCA-2 gradually increased, its internal resistance gradually decreased due to the enhanced contact between conductive carbon skeletons. When the applied stress reached the material's ultimate strength, the resistance mutated and exceeded the threshold (Fig. 5c). This was because exceeding the stress limit triggered catastrophic structural failure, and the resulting collapse of the NFNCA skeleton severed the interconnected conductive pathways, leading to an open-circuit-like state and a sharp rise in resistance. Similar piezoresistive behavior was observed in the transverse direction (Fig. 5d-f).

The gauge factor (*GF*, Eq. S19), defined as the rate of relative resistance change to applied strain, is commonly used to characterize the strain sensitivity of a sensor. The curves of $\Delta R/R_0$ versus compressive strain demonstrated that the sensitivity of NFNCA-2 could be divided into three parts in the longitudinal direction (Fig. 5g). For the strain range of 0-1.3%, the *GF* was maintained at a low level of 0.049. This phenomenon stemmed from the formation of the limited number of discrete contact points during the initial deformation stage, thus leading to low electron transport efficiency. Within the strain range of 1.3%-3.6%, the *GF* value rose markedly to 0.303. This enhanced sensitivity stemmed from the reduction in the distance between the conductive skeletons and the alteration of contact interfaces under compression, thereby effectively regulating the contact resistance and enhancing the electron transmission efficiency. However, as the strain exceeded 3.6%, the *GF* value decreased to 0.015. This decrease could be ascribed to the transformation of the contact mechanism. The initial point contact converted to surface contact, which restricted structural deformation, hindered the formation of new conductive pathways, and thus suppressed electron hopping and transport. Likewise, the sensitivity behavior with three distinct ranges was observed in the transverse direction (Fig. 5h). The *GF* value in the longitudinal direction was higher than that in the transverse direction. This might be due to the fact that the unidirectional structure could create effective conductive pathways along the continuous honeycomb walls in the longitudinal direction, thereby

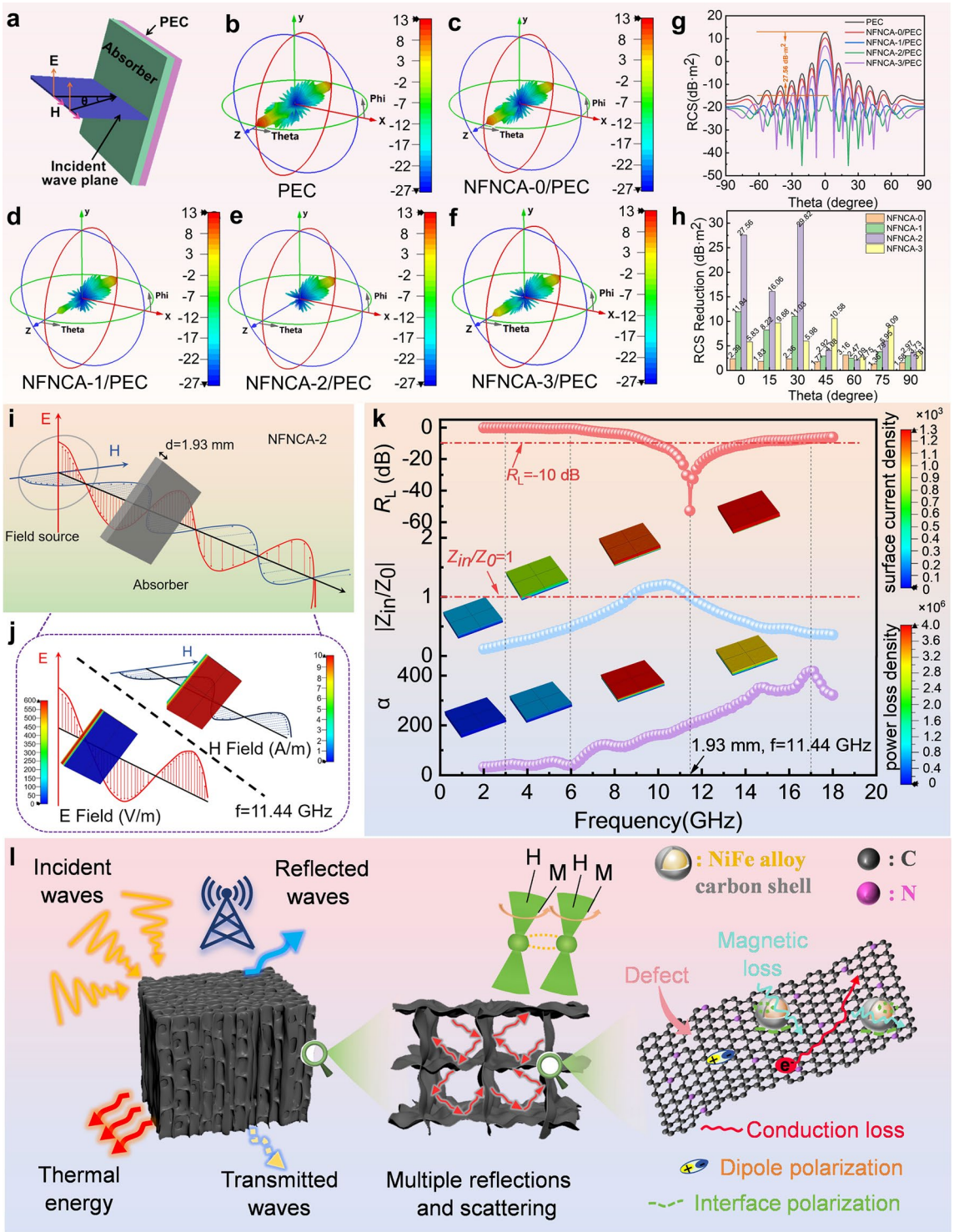

Fig. 4 **a** Sketch of the CST simulation. CST simulation results of **b** PEC, **c** NFNCA-0/PEC, **d** NFNCA-1/PEC, **e** NFNCA-2/PEC, and **f** NFNCA-3/PEC. **g** PEC and NFNCAs/PEC RCS curves in the scattering angle range of 0° ± 90°. **h** RCS reduction values of NFNCAs/PEC. **i** COMSOL simulation model, **j** electric and magnetic field distribution at 11.44 GHz, and **k** comprehensive map of surface current density and power loss density. **l** Schematic diagram of EWA mechanisms for NFNCAs

https://doi.org/10.1007/s40820-026-02128-5

resulting in a higher relative resistance change rate under the same strain [81].

Based on the above results, the internal structure of NFNCA could be monitored by observing the resistance changes, thus realizing real-time monitoring of its structural integrity in operation. This inherent self-sensing capability is highly promising for enhancing the reliability of NFNCA, making it particularly valuable for high-stakes applications such as a lightweight filler in aircraft wings or protective casings for sensitive electronics. In these scenarios, the ability to promptly detect micro-cracks or impact damage in situ and without the need for disassembly is critical for ensuring mission success and preventing catastrophic structural failure.

3.5 Multifunctional Properties

The porous NFNCA-2 exhibited a low density (~ 103.6 mg cm^{-3}) and was sufficiently light, enabling it to stand steadily on the flower petals (Fig. 5i). Moreover, NFNCA-2 could support a load approximately 4000 times its own weight without suffering mechanical damage, demonstrating its excellent mechanical properties (Fig. 5j). The combination of lightweight and robust load ability positioned this novel absorbing material as a prime candidate for structural–functional integrated absorber, with significant potential in sectors such as portable electronics and aerospace. Furthermore, the suppression effect of NFNCA-2 on EMW propagation was verified through two practical application experiments. In the first experiment, an electromagnetic field generated by the Tesla coil formed an electromotive force to light the bulb when switching on the power. However, the bulb went off when placing NFNCA-2 between the coil and the bulb (Fig. 5k). In the second experiment, during the Bluetooth communication test of two smartphones, placing NFNCA-2 over the hole in the tinfoil resulted in signal transmission blockage (Fig. S18, detail in Supporting Information). These phenomena confirmed that NFNCA-2 could provide effective EMW absorption capability for electronic devices.

The porous surface of NFNCA-2 was conducive to multiple reflections and absorption of incident light, and it exhibited excellent photothermal conversion capability. Under simulated solar irradiation (xenon lamp), the photothermal conversion of porous NFNCA-2 was evaluated. Specifically, the equilibrium temperatures of NFNCA-2 were 29.1, 38.7, 54.1, 62.7, and 80.4 °C, respectively, at light power densities of 25, 50, 100, 150, and 200 mW cm^{-2} (Fig. 5l). After switching off the lamp, NFNCA-2 cooled down rapidly to ambient temperature, indicating an efficient and reversible photothermal response. Overall, these findings confirmed the effective thermal management capability of NFNCA and highlighted its considerable potential for applications in electronic devices.

To satisfy the escalating requirements for applications in demanding environments, advanced EMWA materials need to possess multiple functions such as thermal insulation and flame retardancy. The EMWA materials with excellent thermal insulation performance can effectively protect electronic devices from damage caused by overheating or supercooling temperatures [82]. The thermal insulation performance of NFNCA was evaluated using an infrared thermal imager. NFNCA-2 was positioned on two heating stages set at 90 and 130 °C. The material's surface temperature showed a slow upward trend within 20 min (Fig. S19), while stabilizing at 44.5 and 59.4 °C, respectively (Fig. 5m), demonstrating its outstanding thermal insulation performance. In addition, when placed on a copper tray frozen in liquid nitrogen, NFNCA-2 maintained a consistent temperature (11.4 °C) at the top even after 20 min (Figs. 5n and S19). Furthermore, with the extension of freezing time, a thick frost layer formed on the surface of the copper tray beneath the aerogel, while the NFNCA-2 surface was not frozen. Moreover, the area of the palm not covered by NFNCA-2 displayed a different color from the surrounding area and could be clearly distinguished under infrared detection equipment (Fig. S20). In contrast, the area of the palm covered by NFNCA-2 showed the same color as the surrounding area and became invisible under infrared detection equipment. Overall, the remarkable thermal insulation performance endowed NFNCA-2 with effective shield infrared thermal radiation, indicating that it has promising potential in infrared stealth applications.

To further investigate the thermal insulation capability of NFNCA, the flower was placed on the wire gauze insulated with NFNCA-2 (5 mm thickness), followed by heating of the wire gauze using an alcohol lamp. The results demonstrated that after 120 s, both the shape of the flower and the NFNCA-2 were kept almost unchanged (Fig. 5o). For comparison, a thermally conductive copper foam with the same thickness as NFNCA-2 was employed

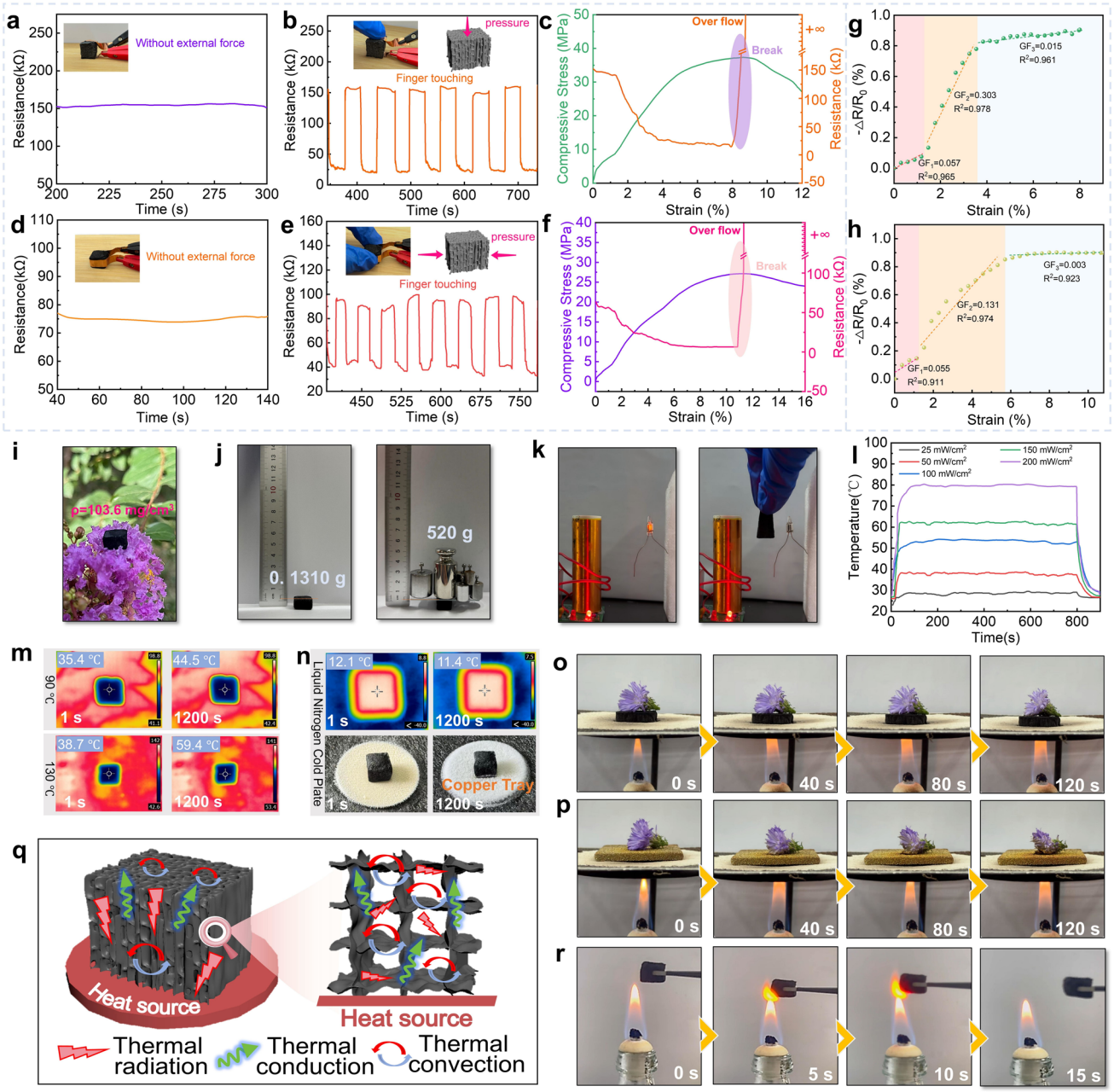

Fig. 5 Multifunctional characteristics of NFNCAs. Resistance-time curves of NFNCA-2 in the longitudinal direction: **a** No external applied force, and **b** slow pressing and releasing with fingers. **c** Stress–strain curves and corresponding resistance changes of NFNCA-2 during compression in the longitudinal direction. Resistance-time curves of NFNCA-2 in the transverse direction: **d** No external applied force, and **e** slow pressing and releasing with fingers. **f** Stress–strain curves and corresponding resistance changes of NFNCA-2 during compression in the transverse direction. *GF* values of NFNCA-2 during compression in the **g** longitudinal and **h** transverse directions. **i** Photograph of NFNCA-2 on the petals. **j** Compression test and **k** Tesla coil test of NFNCA-2. **l** Photothermal temperature curves of NFNCA-2 under different light power densities. **m** Infrared thermal images of NFNCA-2 on 90 °C and 130 °C thermostatic heating plates. **n** Infrared thermal images and optical photographs of NFNCA-2 on the cold plate in liquid nitrogen (-196 °C) at different times. **o, p** Thermal insulation performance of NFNCA-2. **q** Schematic diagram of the thermal insulation mechanism of NFNCA-2. **r** Flame retardancy of NFNCA-2

https://doi.org/10.1007/s40820-026-02128-5

as the control sample and placed between the flower and the heated wire gauze as a thermal conductive medium under the identical heating condition. In this case, the flower was observed to be charred and shrunk into a small piece after 120 s (Fig. 5p). These results revealed that NFNCA had excellent thermal insulation performance, as evidenced by its low thermal conductivity of 0.056 W m^{-1} K^{-1}, along with excellent high-temperature resistance, thus making it a promising candidate for applications in harsh thermal environments. The excellent thermal insulation performance of NFNCA-2 could be attributed to the following reasons. On the one hand, the internal high porosity of NFNCA-2 could reduce the solid-phase thermal conductivity and radiative heat transfer efficiency. On the other hand, the porous structure greatly extended the heat conduction path, and decreased the heat transfer capacity (Fig. 5q) [83].

The flame retardancy of NFNCA was evaluated through alcohol lamp combustion, microscale combustion calorimeter (MCC), and limiting oxygen index (LOI) tests. Notably, NFNCA-2 didn't ignite, with only localized shrinkage and deformation observed at the flame-contact surface in an alcohol lamp for 15 s (Fig. 5r). Furthermore, the MCC test showed that when NFNCA-2 was heated to 850 °C in a N_2/O_2 mixed atmosphere, both the peak heat release rate (PHRR) and heat release capacity (HRC) were detected as zero, and the oxygen consumption during the combustion process was extremely low (only 0.6%) (Table S3). This proved that NFNCA-2 hardly participated in gas-phase combustion reactions, indicating it had excellent flame retardancy and the ability to inhibit combustion spread. Meanwhile, the MCC data revealed that even after a continuous heating process lasting up to 2200 s, the residual carbon content of NFNCA-2 remained as high as 83.8 wt%. The corresponding 16.2 wt% mass loss was attributed to the slight thermal decomposition of NFNCA-2 in a high-temperature air atmosphere. In addition, the LOI was also measured to quantitatively assess flame retardancy. The LOI value of NFNCA-2 was 46.3%, which further confirmed its outstanding flame retardancy. The excellent flame retardancy of NFNCA-2 could be ascribed to the synergistic effect of multiple mechanisms. Firstly, the N-doped carbon matrix could release non-flammable gases (N_2, NH_3) to dilute oxygen and flammable components in the gas phase. Secondly, embedded NiFe nanoparticles could work as catalysts to promote the formation of a dense and stable char layer on the surface of NFNCA-2, which could provide a good physical barrier. Thirdly, the hierarchical porous structure could also dissipate heat and avoid heat accumulation in the material [84–86]. On the whole, the combination of excellent thermal insulation and flame retardancy makes NFNCA more promising for applications in harsh environments.

This work demonstrated a 3D hierarchical biomimetic honeycomb-like porous magnetic NFNCA that integrated radar-infrared stealth, piezoresistive sensing, thermal management, and flame retardancy. Compared with similar reported carbon aerogels [87–98], the advantage of NFNCA-2 lay not in leading every single metric (Table S4) but in achieving the synergistic integration of multiple key functionalities. It retained excellent wave absorption performance, while simultaneously exhibiting outstanding thermal insulation, mechanical stability, flame retardancy, and the real-time structural integrity monitoring capability. Thus, NFNCA represented a more balanced and integrated solution, and its comprehensive multifunctional performance made it far more practically valuable for scenarios requiring synergistic multi-capability integration. The synergistic integrated performance originated from the distinct components (NiFe nanoparticles, N-doped carbon matrix) and honeycomb-like 3D conductive network structure, which were constructed via a rationally designed fabrication strategy combining in situ growth, unidirectional freeze-drying, and pyrolytic carbonization. Overall, this study provides a feasible and efficient strategy to design high-performance carbon-based aerogels for diverse practical applications.

4 Conclusions

In summary, we fabricated biomimetic honeycomb-like porous magnetic NFNCA with low density, high dispersion of magnetic nanoparticles, strong interfacial connectivity, and multifunctionality via a straightforward strategy involving in situ growth, freeze-drying, and pyrolysis carbonization. The rational component design and pore structure of NFNCA resulted in efficient EMWA performance. Benefiting from integrated radar-infrared stealth capabilities, reliable thermal management performance, and superior flame retardancy, NFNCA was an ideal candidate for more complicated and varied environments. Specifically, NFNCA-2 maintained an EAB of 6.24 GHz at 1.60 mm and achieved a minimum R_L value of −53.49 dB as well as a specific R_L value of −138.58 dB mm^{-1} at 1.93 mm. COMSOL simulations

confirmed the effectiveness of NFNCA in reducing radar scattering intensity and its potential for practical applications. Interestingly, the 3D cross-linked conductive network of NFNCA-2 with a high graphitization degree could serve as strain sensors to monitor the structural integrity of materials in real-time, thus avoiding potential safety hazards. Furthermore, the rapid photothermal conversion of NFNCA-2 confirmed its excellent thermal management ability. Meanwhile, the outstanding thermal insulation capability and flame retardancy of NFNCA-2 enabled its practical application in high-temperature conditions. With high performance, facile fabrication, and multifunctionality, NFNCA holds broad and promising application prospects in fields such as electromagnetic compatibility and protection, electronic devices, thermal management, real-time self-sensing structural health monitoring, and aerospace.

Acknowledgements This work was financially supported by the Key Research and Development Project of Shaanxi Province (2024GX-YBXM-381), the Open Fund Project of Hunan Provincial Key Laboratory of Water Treatment Functional Materials (No. KFJJ2403), and the National Natural Science Foundation of China (No. 21978162).

Author Contributions Xiaosen Du contributed to conceptualization, methodology, validation, formal analysis, investigation, data curation, and writing—original draft. Jianhua Zhou contributed to writing—review and editing, project administration, and funding acquisition. Jiarui Yu contributed to visualization. Xiaoyan Nie, Mingyu Luo and Xingyuan He contributed to resources. Anguo Xiao contributed to supervision.

Declarations

Conflict of interest The authors declare no interest conflict. They have no known competing financial interests or personal relationships that could have appeared to influence the work reported in this paper.

Supplementary Information The online version contains supplementary material available at https://doi.org/10.1007/s40820-026-02128-5.

References

1. X. Zhou, P. Min, Y. Liu, M. Jin, Z.-Z. Yu et al., Insulating electromagnetic-shielding silicone compound enables direct potting electronics. Science **385**(6714), 1205–1210 (2024). https://doi.org/10.1126/science.adp6581
2. G. Kang, G. Kwon, J. Jeon, J. Kwon, M.-K. Kim et al., Electromagnetic interference shielding using metal and MXene thin films. Nature **647**(8089), 356–363 (2025). https://doi.org/10.1038/s41586-025-09699-0
3. C.-Z. Qi, P. Min, X. Zhou, M. Jin, X. Sun et al., Multifunctional asymmetric bilayer aerogels for highly efficient electromagnetic interference shielding with ultrahigh electromagnetic wave absorption. Nano-Micro Lett. **17**(1), 291 (2025). https://doi.org/10.1007/s40820-025-01800-6
4. Y. Zhou, Y. Zhang, K. Ruan, H. Guo, M. He et al., MXene-based fibers: preparation, applications, and prospects. Sci. Bull. **69**(17), 2776–2792 (2024). https://doi.org/10.1016/j.scib.2024.07.009
5. Y.H. Jin, J.-H. Han, J. Park, M. Kim, S.-H. Seok et al., Water- and oxidation-resistant MXenes for advanced electromagnetic interference shielding applications. InfoMat **7**(9), e70034 (2025). https://doi.org/10.1002/inf2.70034
6. X. Zeng, X. Jiang, Y. Ning, Y. Gao, R. Che, Constructing built-in electric fields with semiconductor junctions and Schottky junctions based on Mo-MXene/Mo-metal sulfides for electromagnetic response. Nano-Micro Lett. **16**(1), 213 (2024). https://doi.org/10.1007/s40820-024-01449-7
7. H. Sun, B. Yang, M. Zhang, Functional–structural integrated aramid nanofiber-based honeycomb materials with ultrahigh strength and multi-functionalities. Adv. Fiber Mater. **6**(4), 1122–1137 (2024). https://doi.org/10.1007/s42765-024-00411-x
8. K.-B. Cui, C.-L. He, J.-H. Wu, X. Gao, Y. Li et al., Multispectrum electromagnetic response in FeNiHo/C heterodimensional structure for microwave absorption and multimode photodetection. Adv. Mater. **37**(44), e10507 (2025). https://doi.org/10.1002/adma.202510507
9. B. Zhan, Y. Qu, X. Qi, J. Ding, J.-J. Shao et al., Mixed-dimensional assembly strategy to construct reduced graphene oxide/carbon foams heterostructures for microwave absorption, anti-corrosion and thermal insulation. Nano-Micro Lett. **16**(1), 221 (2024). https://doi.org/10.1007/s40820-024-01447-9
10. Z. Zhang, J. Wang, J. Shang, Y. Xu, Y.-J. Wan et al., A through-thickness arrayed carbon fibers elastomer with horizontal segregated magnetic network for highly efficient thermal management and electromagnetic wave absorption. Small **19**(4), 2205716 (2023). https://doi.org/10.1002/smll.202205716

11. P. Zhang, Q. Wei, J. Su, X. Guo, P.K. Shen et al., Strengthening the d-p orbital hybridization of N-doped carbon nanocages with encapsulated Fe nanoparticles for efficient electromagnetic wave absorption. Chem. Eng. J. **516**, 163716 (2025). https://doi.org/10.1016/j.cej.2025.163716
12. T.-T. Liu, L.-Y. Li, P. Gao, L. Li, M.-S. Cao, High-entropy electromagnetic functional materials: from electromagnetic genes to materials design. Mater. Sci. Eng. R. Rep. **164**, 100982 (2025). https://doi.org/10.1016/j.mser.2025.100982
13. M. Shen, X. Li, J. Qi, J. Sun, W. Cao et al., Magnetic metal-loaded wood carbon aerogel composites for electromagnetic shielding and microwave absorption. Compos. Part A Appl. Sci. Manuf. **198**, 109070 (2025). https://doi.org/10.1016/j.compositesa.2025.109070
14. K. Xu, Y. Jiao, J. Li, H. Xiao, Q. Fu, FeP nanoparticle embedded in N, P-doped 3D porous wood-derived carbon aerogel for oxygen reduction reaction. Carbon **228**, 119408 (2024). https://doi.org/10.1016/j.carbon.2024.119408
15. Y. Zhang, P. Zhu, H. Sun, X. Sun, Y. Ye et al., Superelastic cellulose sub-micron fibers/carbon black aerogel for highly sensitive pressure sensing. Small **20**(13), 2310038 (2024). https://doi.org/10.1002/smll.202310038
16. H. Liu, T. Xu, Q. Liang, Q. Zhao, D. Zhao et al., Compressible cellulose nanofibrils/reduced graphene oxide composite carbon aerogel for solid-state supercapacitor. Adv. Compos. Hybrid Mater. **5**(2), 1168–1179 (2022). https://doi.org/10.1007/s42114-022-00427-0
17. L. Pei, F. Ren, S. Yuan, C. Li, D. Zhang et al., Lightweight Co@MXene/cellulose-derived carbon aerogel for electromagnetic shielding and absorption capacity. ACS Appl. Nano Mater. **8**(39), 18905–18913 (2025). https://doi.org/10.1021/acsanm.5c03312
18. S. Wang, X. Zhang, S. Hao, J. Qiao, Z. Wang et al., Nitrogen-doped magnetic-dielectric-carbon aerogel for high-efficiency electromagnetic wave absorption. Nano-Micro Lett. **16**(1), 16 (2023). https://doi.org/10.1007/s40820-023-01244-w
19. Y. Chen, J. Luo, C. Xue, Z. Huang, M. He et al., Self-assembled nanostructures of 0D ZnO on 3D chitin-derived carbon aerogel for wideband electromagnetic wave absorption. Carbon **241**, 120382 (2025). https://doi.org/10.1016/j.carbon.2025.120382
20. X. Du, J. Zhou, J. Yu, C.-H. Xue, Biomimetic coral-like Ni/N-doped carbon aerogel derived from self-assembly of MOF and collagen protofibril for high-efficiency microwave attenuation and thermal management. Chem. Eng. J. **516**, 164054 (2025). https://doi.org/10.1016/j.cej.2025.164054
21. J. Zhou, J. Yu, M. Zhou, X. Wang, Anisotropic MXene@polydopamine- and dialdehyde carboxymethyl cellulose-modified collagen aerogel supported form-stable phase change composites for light-to-heat conversion and energy storage. Biomacromol **25**(10), 6451–6464 (2024). https://doi.org/10.1021/acs.biomac.4c00529
22. H. Wang, Advantages of animal leather over alternatives and its medical applications. Eur. Polym. J. **214**, 113153 (2024). https://doi.org/10.1016/j.eurpolymj.2024.113153
23. J. Ma, T. Ma, Q. Fan, Y. Shen, M. Liu et al., Harnessing the reversible reaction principle: a novel Zr-based halide Perovskite tanning system for effective Zr^{4+} penetration in the leather collagen. Int. J. Biol. Macromol. **321**, 146468 (2025). https://doi.org/10.1016/j.ijbiomac.2025.146468
24. Z. He, L. Shi, R. Sun, L. Ding, M. He et al., Low-temperature oxidation induced phase evolution with gradient magnetic heterointerfaces for superior electromagnetic wave absorption. Nano-Micro Lett. **17**(1), 7 (2024). https://doi.org/10.1007/s40820-024-01516-z
25. W. Luo, R. Chi, F. Zeng, Y. Wu, Y. Chen et al., Multilayer structure ammoniated collagen fibers for fast adsorption of anionic dyes. ACS Omega **6**(41), 27070–27079 (2021). https://doi.org/10.1021/acsomega.1c03643
26. M. Xu, C. Yue, M. Hu, M. Liao, R. Zhang et al., Tannic acid-mediated multifunctional collagen/cellulose nanofiber composite aerogels for sustained drug release, antibacterial properties, and hemostasis. ACS Appl. Polym. Mater. **7**(15), 9750–9763 (2025). https://doi.org/10.1021/acsapm.5c01302
27. M. Yu, Y. Han, J. Li, L. Wang, Magnetic N-doped carbon aerogel from sodium carboxymethyl cellulose/collagen composite aerogel for dye adsorption and electrochemical supercapacitor. Int. J. Biol. Macromol. **115**, 185–193 (2018). https://doi.org/10.1016/j.ijbiomac.2018.04.012
28. S. Zhang, C. Wang, X. Meng, S. Liu, X. Li et al., Enhanced electromagnetic wave absorption of multicore Fe_4N@N-doped porous carbon core-shell microspheres through dielectric-magnetic coordination. Carbon **237**, 120176 (2025). https://doi.org/10.1016/j.carbon.2025.120176
29. H. Jiang, Y. Wang, C. Wang, Y. Feng, D. Yang et al., Bamboo-like carbon nanotubes assisted assembly of magnetic-dielectric aerogels to enhance microwave attenuation. Carbon **234**, 119973 (2025). https://doi.org/10.1016/j.carbon.2024.119973
30. K. Song, Y.-T. Pan, J. Zhang, P. Song, J. He et al., Metal–organic frameworks–based flame-retardant system for epoxy resin: a review and prospect. Chem. Eng. J. **468**, 143653 (2023). https://doi.org/10.1016/j.cej.2023.143653
31. C. Zheng, M. Ning, Z. Zou, G. Lv, Q. Wu et al., Two birds with one stone: broadband electromagnetic wave absorption and anticorrosion performance in 2-18 GHz for Prussian blue analog derivatives aimed for practical applications. Small **19**(32), e2208211 (2023). https://doi.org/10.1002/smll.202208211
32. C. Wang, X. Lin, C. Hu, Y. Ding, Z. Wang et al., Bio-based derived carbon materials for permittivity metamaterials: dual efficacy of electromagnetic wave protection and Joule heating. Mater. Horiz. **12**(16), 6349–6362 (2025). https://doi.org/10.1039/d5mh00379b
33. Y. Zheng, P. Wu, Y. Dou, W. Jiang, S. Xia et al., Hawthorn snowball–shaped FeCo/Cl-codoped biomass-derived porous carbon microspheres for efficient electromagnetic wave absorption. Chem. Eng. J. **522**, 167970 (2025). https://doi.org/10.1016/j.cej.2025.167970
34. L. Shao, X. Li, Y. Wang, G. Xia, F. Fan et al., Interface engineering optimization: *in-situ* growth NiZn/carbon aerogel composite for high-performance microwave absorption.

Carbon **242**, 120459 (2025). https://doi.org/10.1016/j.carbon.2025.120459

35. J. Qiao, Q. Song, X. Zhang, S. Zhao, J. Liu et al., Enhancing interface connectivity for multifunctional magnetic carbon aerogels: an *in situ* growth strategy of metal-organic frameworks on cellulose nanofibrils. Adv. Sci. **11**(19), 2400403 (2024). https://doi.org/10.1002/advs.202400403
36. K. Yang, G. Song, Y. Li, Q. An, S. Zhai et al., Transforming *in-situ* grown chitosan/ZIF-67 aerogels into 3D N-doped Co/CoO/carbon composites for improved electromagnetic wave absorption. J. Alloys Compd. **936**, 168195 (2023). https://doi.org/10.1016/j.jallcom.2022.168195
37. S. Liu, S. Wang, M. Sang, J. Zhou, J. Zhang et al., Nacre-mimetic hierarchical architecture in polyborosiloxane composites for synergistically enhanced impact resistance and ultra-efficient electromagnetic interference shielding. ACS Nano **16**(11), 19067–19086 (2022). https://doi.org/10.1021/acsnano.2c08104
38. H. Joukhdar, A. Seifert, T. Jüngst, J. Groll, M.S. Lord et al., Ice templating soft matter: fundamental principles and fabrication approaches to tailor pore structure and morphology and their biomedical applications. Adv. Mater. **33**(34), 2100091 (2021). https://doi.org/10.1002/adma.202100091
39. Z. Yang, H. Lv, R. Wu, Rational construction of graphene oxide with MOF-derived porous NiFe@C nanocubes for high-performance microwave attenuation. Nano Res. **9**(12), 3671–3682 (2016). https://doi.org/10.1007/s12274-016-1238-z
40. Z. Ye, Y. Xia, R. Luo, H. Yang, Y. Liu et al., Effect of $NiFe_2O_4$ filler on the wave-absorbing properties of PIP-SiC/SiCN composites. Chem. Eng. J. **521**, 166976 (2025). https://doi.org/10.1016/j.cej.2025.166976
41. Y. Li, H. Wei, L. Chen, C. Xie, H. Ding et al., Regulating the electronic structure of MAX phases based on rare earth element Sc to enhance electromagnetic wave absorption. ACS Nano **18**(14), 10019–10030 (2024). https://doi.org/10.1021/acsnano.3c11585
42. W. He, J. Zheng, W. Dong, S. Jiang, G. Lou et al., Efficient electromagnetic wave absorption and Joule heating *via* ultralight carbon composite aerogels derived from bimetal-organic frameworks. Chem. Eng. J. **459**, 141677 (2023). https://doi.org/10.1016/j.cej.2023.141677
43. C. Gong, J. Ding, C. Wang, Y. Zhang, H. Cong et al., Utilizing Se vacancies as electronic traps to synergize impedance matching and dipole polarization with ultrathin strategy to boost Fe-Se electromagnetic wave absorption. Chem. Eng. J. **480**, 147793 (2024). https://doi.org/10.1016/j.cej.2023.147793
44. Y. Guo, Y. Zhu, J. Sun, Y. Lin, X. Li et al., MOF-derived carbon nanotube bridged Co/MoC@NC composites for enhanced electromagnetic wave absorption. J. Alloys Compd. **1010**, 177346 (2025). https://doi.org/10.1016/j.jallcom.2024.177346
45. Y. Gao, Q. Wu, X. Jia, L. Pan, C. Li et al., Orientation architecture engineering for enhanced electromagnetic wave absorption and active–passive infrared camouflage performances. Adv. Funct. Mater. **35**(40), 2508442 (2025). https://doi.org/10.1002/adfm.202508442
46. L. Xue, E. He, D. Wang, L. Yu, X. Yan, Enhanced electromagnetic wave absorption performance of ZnO/N-doped carbon microspheres in 2–18 GHz. Vacuum **213**, 112156 (2023). https://doi.org/10.1016/j.vacuum.2023.112156
47. M. Liu, W. Jiang, X. Jiang, L. Yu, Nitrogen-doped lychee-like saccharide-based carbon microspheres with high-performance microwave absorption. Diam. Relat. Mater. **142**, 110725 (2024). https://doi.org/10.1016/j.diamond.2023.110725
48. Z. Wang, K. Yang, H. Wang, J. Zhao, P. Liu, CNTs decorated Fe_3O_4/Co–Ni polyhedrons with heterogeneous interfaces for promoting microwave absorption. Compos. Commun. **49**, 101976 (2024). https://doi.org/10.1016/j.coco.2024.101976
49. H. Jiang, Z. Chen, J. Tao, X. Zhang, Z. Wang et al., Phase interface manipulation by adjusting atomic ordering in metal-organic framework to facilitate microwave absorption. Carbon **212**, 118107 (2023). https://doi.org/10.1016/j.carbon.2023.118107
50. R. Cai, P.-A. Yang, H. Ruan, X. Huang, Z. Zhou et al., Directional control of electromagnetic parameters of Fe@Ni nanowires for ultrathin and low-frequency microwave absorbing. Appl. Surf. Sci. **668**, 160434 (2024). https://doi.org/10.1016/j.apsusc.2024.160434
51. J. Ren, Y. Lyu, Z. Liu, M. Ahmad, Q. Zhang et al., Microwave absorption performance evaluation of carbonized derivatives of Fe_3O_4@MOF-74 with controllable morphologies. ACS Appl. Electron. Mater. **4**(11), 5221–5233 (2022). https://doi.org/10.1021/acsaelm.2c00900
52. J. Liu, C. Liu, Y. Tong, H. Sun, H. Peng et al., Enhanced EMW absorption properties of SiCN/Fe/Ni ceramics modified with Fe/Ni bimetal. Ceram. Int. **48**(20), 30206–30217 (2022). https://doi.org/10.1016/j.ceramint.2022.06.293
53. Z. Shen, Y. Zu, S. Ma, Y. Chen, Z. Zhang et al., Controllable synthesis of porous carbon@ $Fe_{20}Ni_{80}$ composites with improved microwave absorption performance. Compos. Part B Eng. **259**, 110710 (2023). https://doi.org/10.1016/j.compositesb.2023.110710
54. C. Li, L. Liang, B. Zhang, Y. Yang, G. Ji, Synergistic customization of interfacial engineering MXene-integrated aerogels enable multifunctional radar-infrared stealth. Chem. Eng. J. **520**, 166211 (2025). https://doi.org/10.1016/j.cej.2025.166211
55. X. Han, Y. Feng, N. Zhang, W. Du, W. Zhang et al., Bio-based multifunctional carbon aerogels for ultrawide electromagnetic wave absorption and thermal insulation. Carbon **238**, 120231 (2025). https://doi.org/10.1016/j.carbon.2025.120231
56. X. He, H. Jia, L. He, R. Wang, W. Ye et al., SiO_2 aerogel-encapsulated and multilayer carbon-magnetic heterostructure-reinforced carbon felt for high-efficiency EM wave absorption and thermal insulation. Chem. Eng. J. **524**, 169293 (2025). https://doi.org/10.1016/j.cej.2025.169293
57. Q. Xu, X. Zhu, J. Yu, Y. Xie, Y. Yu et al., Constructing core-shell structural bimetallic CoNi alloys doped carbon aerogels for highly efficient electromagnetic wave absorption. J. Alloys Compd. **1015**, 178854 (2025). https://doi.org/10.1016/j.jallcom.2025.178854

 https://doi.org/10.1007/s40820-026-02128-5

58. T. Tian, W. Liao, Joint carbon aerogel of waste polyester-cotton blends and waste lithium-ion battery towards effective electromagnetic wave absorption and infrared stealth. J. Environ. Chem. Eng. **14**(1), 120902 (2026). https://doi.org/10.1016/j.jece.2025.120902
59. Z. Qu, C. Hu, P. Zhang, H. Wang, Y. Ye et al., Lightweight graphene-based composite aerogels for efficient electromagnetic wave absorption at high temperatures. Ceram. Int. **51**(30), 65015–65024 (2025). https://doi.org/10.1016/j.ceramint.2025.11.063
60. Z. liu, L. Wang, Y. Zhao, J. Ren, H. Wang et al., Environmental adaptability and efficient electromagnetic wave protection of C/Co aerogels by anchoring Co to biomass carbon *via* the high-temperature induced morphological transformation of ZIF-67. Nano Res. **18**(8), 94907581 (2025). https://doi.org/10.26599/nr.2025.94907581
61. T. Zheng, H. Yu, J. Ruan, H. Wang, X. Shi et al., Ultralow-loading CoNi-MOF enables ultralight graphene aerogels with superior electromagnetic wave absorption. Appl. Surf. Sci. **714**, 164491 (2025). https://doi.org/10.1016/j.apsusc.2025.164491
62. R. Xu, M. He, H. Li, S. Feng, Y. Wang et al., Multi-scale Co-MOF derived Co-N/C@graphene hybrid aerogel for effective electromagnetic wave absorption. Synth. Met. **313**, 117909 (2025). https://doi.org/10.1016/j.synthmet.2025.117909
63. W. Gu, X. Tan, Z. Luo, Z. Chen, C. Sun et al., Environmentally-friendly $CoxNi_y$/carbon hybrid aerogels with dielectric and magnetic coupling network for highly efficient radar/infrared compatibility. Carbon **248**, 121126 (2026). https://doi.org/10.1016/j.carbon.2025.121126
64. M. Zheng, F. Liu, D. Yang, C. Chen, X. Dong et al., Chitosan-intercalated rectorite/biomass carbon aerogels with enhanced heterogeneous interfaces for broadband microwave absorption. Chem. Eng. J. **519**, 165579 (2025). https://doi.org/10.1016/j.cej.2025.165579
65. F. Yin, H. Lin, W. Wang, L. Zhao, R. Paul et al., Multifunctional anisotropic aerogels for intelligent electromagnetic wave absorption. Adv. Funct. Mater. **35**(14), 2418257 (2025). https://doi.org/10.1002/adfm.202418257
66. J. Qiao, Q. Song, L. Xuan, J. Liu, X. Zhang et al., Dual cross-linked magnetic MXene aerogel with high strength and durability enables multifunctionality. Adv. Funct. Mater. **34**(33), 2401687 (2024). https://doi.org/10.1002/adfm.202401687
67. W. Li, W. Li, Z. Ma, Y. Kang, T. Zou et al., N atoms regulate heterogeneous crystal phase engineering of mesoporous magnetic Fe_xN nanofibers to promote electromagnetic wave dissipation of magnetic composite aerogel absorbers. Chem. Eng. J. **481**, 148584 (2024). https://doi.org/10.1016/j.cej.2024.148584
68. A. Cui, C. Wang, Y. Miao, X. Wang, Y. Wang et al., B─C bonding configuration manipulation strategy toward synergistic optimization of polarization loss and conductive loss for highly efficient electromagnetic wave absorption. Adv. Funct. Mater. **35**(15), 2420292 (2025). https://doi.org/10.1002/adfm.202420292
69. H. Wang, F. Meng, F. Huang, C. Jing, Y. Li et al., Interface modulating CNTs@PANi hybrids by controlled unzipping of the walls of CNTs to achieve tunable high-performance microwave absorption. ACS Appl. Mater. Interfaces **11**(12), 12142–12153 (2019). https://doi.org/10.1021/acsami.9b01122
70. B. Wang, H. Wu, W. Hou, Z. Fang, H. Liu et al., Optimizing dielectric polarization for electromagnetic wave attenuation *via* an enhanced Maxwell–Wagner–Sillars effect in hollow carbon microspheres. J. Mater. Chem. A **11**(43), 23498–23510 (2023). https://doi.org/10.1039/d3ta05647c
71. J. Qiao, X. Zhang, C. Liu, L. Lyu, Z. Wang et al., Facile fabrication of Ni embedded TiO_2/C core-shell ternary nanofibers with multicomponent functional synergy for efficient electromagnetic wave absorption. Compos. Part B Eng. **200**, 108343 (2020). https://doi.org/10.1016/j.compositesb.2020.108343
72. Z. Tang, L. Xu, C. Xie, L. Guo, L. Zhang et al., Synthesis of $CuCo_2S_4$@expanded graphite with crystal/amorphous heterointerface and defects for electromagnetic wave absorption. Nat. Commun. **14**(1), 5951 (2023). https://doi.org/10.1038/s41467-023-41697-6
73. C. Chen, Z. Shan, S. Tao, A. Xie, H. Yang et al., Atomic tuning in electrically conducting bimetallic organic frameworks for controllable electromagnetic wave absorption. Adv. Funct. Mater. **33**(45), 2305082 (2023). https://doi.org/10.1002/adfm.202305082
74. B. Zhao, Y. Du, H. Lv, Z. Yan, H. Jian et al., Liquid-metal-assisted programmed galvanic engineering of core–shell nanohybrids for microwave absorption. Adv. Funct. Mater. **33**(34), 2302172 (2023). https://doi.org/10.1002/adfm.202302172
75. R. Cui, Y. Li, X. Zhang, Z. Duan, B. Zhao et al., Controlled deintercalation of graphene/organic superlattices with dense atomic-scale steric Schottky heterojunctions for extreme microwave absorption. Nat. Commun. **16**(1), 5804 (2025). https://doi.org/10.1038/s41467-025-60707-3
76. B. Zhao, Y. Du, Z. Yan, L. Rao, G. Chen et al., Structural defects in phase-regulated high-entropy oxides toward superior microwave absorption properties. Adv. Funct. Mater. **33**(1), 2209924 (2023). https://doi.org/10.1002/adfm.202209924
77. B. Zhao, Z. Yan, Y. Du, L. Rao, G. Chen et al., High-entropy enhanced microwave attenuation in titanate perovskites. Adv. Mater. **35**(11), e2210243 (2023). https://doi.org/10.1002/adma.202210243
78. R. Cui, Z. Duan, Y. Li, X. Zhang, X. Liu et al., High-temperature oxide ceramic microwave absorber enabled by thermionic migration mediated by electron delocalization. Nat. Commun. **16**(1), 9179 (2025). https://doi.org/10.1038/s41467-025-64208-1
79. B. Zhao, Z. Yan, L. Liu, Y. Zhang, L. Guan et al., A liquid-metal-assisted competitive galvanic reaction strategy toward indium/oxide core-shell nanoparticles with enhanced microwave absorption. Adv. Funct. Mater. **34**(18), 2314008 (2024). https://doi.org/10.1002/adfm.202314008
80. Y. Du, Z. Yan, W. You, Q. Men, G. Chen et al., Balancing MXene surface termination and interlayer spacing enables

superior microwave absorption. Adv. Funct. Mater. **33**(34), 2301449 (2023). https://doi.org/10.1002/adfm.202301449

81. M. Xie, G. Qian, Y. Yu, C. Chen, H. Li et al., High-performance flexible reduced graphene oxide/polyimide nanocomposite aerogels fabricated by double crosslinking strategy for piezoresistive sensor application. Chem. Eng. J. **480**, 148203 (2024). https://doi.org/10.1016/j.cej.2023.148203
82. W. Luo, X. Jiang, Y. Liu, X. Yuan, J. Huo et al., Entropy-driven morphology regulation of MAX phase solid solutions with enhanced microwave absorption and thermal insulation performance. Small **20**(8), 2305453 (2024). https://doi.org/10.1002/smll.202305453
83. Y. Zhou, Y. Zhang, Y. Pang, H. Guo, Y. Guo et al., Thermally conductive $Ti_3C_2T_x$ fibers with superior electrical conductivity. Nano-Micro Lett. **17**(1), 235 (2025). https://doi.org/10.1007/s40820-025-01752-x
84. C. Cui, L. Geng, S. Jiang, W. Bai, L. Dai et al., Architecture design of a bamboo cellulose/Nb_2CT_x MXene/ZIF-67-derived lightweight Co/Nb_2CT_x/carbon aerogel for highly efficient electromagnetic wave absorption, thermal insulation, and flame retardant. Ind. Eng. Chem. Res. **62**(21), 8297–8311 (2023). https://doi.org/10.1021/acs.iecr.3c00534
85. S. Xu, J. Liu, X. Liu, H. Li, X. Gu et al., Preparation of Ni-Fe layered double hydroxides and its application in thermoplastic polyurethane with flame retardancy and smoke suppression. Polym. Degrad. Stab. **202**, 110043 (2022). https://doi.org/10.1016/j.polymdegradstab.2022.110043
86. F. Guo, Y. Zhang, L. Cai, L. Li, NiFe Prussian blue analogue nanocages decorated magnesium hydroxide rod for enhancing fire safety and mechanical properties of epoxy resin. Compos. Part B Eng. **233**, 109650 (2022). https://doi.org/10.1016/j.compositesb.2022.109650
87. M. Zhang, L. Chen, Z. Ding, Z. Zhao, C. Jiang, Enhanced microwave absorption performance of lightweight, heat-insulating and flame retardant CoMo-LDO@Co/C aerogel through multiphase heterojunctions engineering and synergistic effect. Carbon **247**, 121084 (2026). https://doi.org/10.1016/j.carbon.2025.121084
88. Q. Peng, W. Yu, C. Gao, L. Geng, P. Fatehi et al., The synergistic effect of hybridization-micro/nano-structural design on the Ti_3C_2Tx MXene@CoFe-MOF@chitosan heterojunction enhances the absorption of electromagnetic waves. Adv. Compos. Hybrid Mater. **8**(2), 232 (2025). https://doi.org/10.1007/s42114-025-01305-1
89. F. Wu, P. Hu, F. Hu, Z. Tian, J. Tang et al., Multifunctional MXene/C aerogels for enhanced microwave absorption and thermal insulation. Nano-Micro Lett. **15**(1), 194 (2023). https://doi.org/10.1007/s40820-023-01158-7
90. H. Wu, X. Ren, W. Hu, Y. Tang, H. Yin et al., Permittivity controllable CNTs/PI composite aerogels with oriented microchannels for advanced microwave absorption and thermal isolation. Carbon **233**, 119883 (2025). https://doi.org/10.1016/j.carbon.2024.119883
91. Z. Jin, X. Feng, Y. Hou, H. Zhu, L. Wang, Lightweight and thermally insulating ZnO/SiCnw aerogel: a promising high temperature electromagnetic wave absorbing material with oxidation resistance. Chem. Eng. J. **498**, 155110 (2024). https://doi.org/10.1016/j.cej.2024.155110
92. D. Yang, S. Dong, T. Cui, J. Xin, Y. Xie, G. Chen, C. Hong, X. Zhang, Lightweight and robust electrospun zirconia fiber reinforced carbon aerogel composites for efficient microwave absorption and heat insulation. Carbon **228**, 119387 (2024). https://doi.org/10.1016/j.carbon.2024.119387
93. J. Jiang, Y. Xue, J. Li, C. Zhang, X. Hu et al., Microwave absorption and thermal insulation integrated polymer-derived SiBCN/SiBCNnf ceramic aerogel with enhanced mechanical property. Ceram. Int. **50**(21), 41527–41533 (2024). https://doi.org/10.1016/j.ceramint.2024.08.002
94. T. Liu, Y. Zhang, C. Wang, Y. Kang, M. Wang, F. Wu, W. Huang, Multifunctional MoCx hybrid polyimide aerogel with modified porous defect engineering for highly efficient electromagnetic wave absorption. Small **20**(31), 2308378 (2024). https://doi.org/10.1002/smll.202308378
95. Y.-F. Kang, J.-L. Tang, M. Song, W. Wang, J.-C. Ma, Z.-Y. Ji, T. Liu, W.-H. Huang, Electrostatic encapsulation of cobalt ions into crystalline framework derived polymer aerogel: ultra-light, pressure resistant, hydrophobic, photothermal conversion, heat insulation and infrared stealth. Chin. J. Polym. Sci. **42**(7), 946–957 (2024). https://doi.org/10.1007/s10118-024-3111-y
96. M. Chao, N. Chu, B. Zhang, C. Luo, L. Yan, MXene/carbon fiber/polyimide composite aerogel for multifunctional microwave absorption. Compos. Commun. **46**, 101837 (2024). https://doi.org/10.1016/j.coco.2024.101837
97. D. Yang, S. Dong, J. Xin, C. Liu, P. Hu, L. Xia, C. Hong, X. Zhang, Robust and thermostable C/SiOC composite aerogel for efficient microwave absorption, thermal insulation and flame retardancy. Chem. Eng. J. **469**, 143851 (2023). https://doi.org/10.1016/j.cej.2023.143851
98. D. Yang, S. Dong, T. Cui, J. Xin, X. Xu et al., Multifunctional carbon fiber reinforced C/SiOC aerogel composites for efficient electromagnetic wave absorption, thermal insulation, and flame retardancy. Small **20**(23), 2308145 (2024). https://doi.org/10.1002/smll.202308145

 https://doi.org/10.1007/s40820-026-02128-5